Journal of Solid State Chemistry 185 (2012) 253–263

Contents lists available at SciVerse ScienceDirect

Journal of Solid State Chemistry

journal homepage: www.elsevier.com/locate/jssc

Two types of rare earth–organic frameworks constructed by racemic tartaric acid

Zhan-Guo Jiang [a], Yao-Kang Lv [a,b], Jian-Wen Cheng [a], Yun-Long Feng [a,*]

[a] Zhejiang Key Laboratory for Reactive Chemistry on Solid Surfaces, Institute of Physical Chemistry, Zhejiang Normal University, Jinhua, Zhejiang 321004, PR China
[b] Department of Chemistry, Tongji University, 1239 Siping Road, Shanghai 200092, PR China

ARTICLE INFO

Article history:
Received 17 July 2011
Received in revised form
27 October 2011
Accepted 7 November 2011
Available online 18 November 2011

Keywords:
Rare complex
Racemic saccharic acid
Topology
Photoluminescence

ABSTRACT

Hydrothermal reactions of rare earth oxides with racemic tartaric acid (H_2tar) yielded 7 rare earth(III) MOFs with general formulas $[R_2(tar)_3(H_2O)_2]_n$ (R=Y (**1**), Sm (**4**), Eu (**5**), Tb (**6**), Dy (**7**)) and $[R_2(tar)_2(C_2O_4)(H_2O)_2]_n \cdot 4nH_2O$ (R=La (**2**), Nd (**3**)). X-ray powder diffraction analysis and single-crystal X-ray diffraction analysis reveal that they present two different structural types. MOFs **1**, **4**, **5**, **6** and **7** are isostructural and crystallize in the orthorhombic non-centrosymmetric space group *Iba*2, and feature unusual **fsc**-3,4-*Iba*2 topology. MOFs **2** and **3** are isostructural and crystallize in monoclinic $P2_1/c$ space group and display rare **fsx**-4,5-$P2_1/c$ topology containing hydrophilic channels bounded by triple helical chains along *a* axis. MOFs **3**, **4**, **5**, **6** and **7** exhibit intense lanthanide characteristic photoluminescence at room temperature.

1. Introduction

Nowadays, much interest in the designed synthesis of metal-organic frameworks (MOFs), which have achieved considerable progress in material chemistry and supramolecular chemistry [1], is driven by their potential properties for eventual application and intriguing topology architecture [2]. It is definite that hydrothermal synthesis has been one of the powerful techniques for the synthesis of new MOFs with diverse architectures. Under relatively high temperature and pressure, the problems associated with solubility can be well solved; thus the reactivity of reactants in the crystallization process is efficiently enhanced [3]. This technique has earned enormous importance due to its simplicity and the tremendous results regarding the production of MOFs [4]. The hydrothermal reactions are affected by a variety of parameters such as reaction time, temperature and pH value [5]; these reactions are often quite complicated and may involve in situ hydrolysis, oxidation, and ligand synthesis [6]. Although it is not always possible to exert synthetic control, during the last two decades, a fascinating variety of novel MOFs has been obtained from hydrothermal reactions. Inspired by the aforementioned considerations, we aimed to obtain new MOFs via linking metal cations with multicarboxylic organic ligands through hydrothermal synthesis [7]. Racemic tartaric acid (H_2tar) as an excellent candidate is a cheap hydroxy dicarboxylic acid and has six coordination sites which are helpful to get high dimensional structure. Rare earth MOFs have attracted considerable attention as promising sensory materials due to their unique coordination chemistry and intense luminescence with long excited-state lifetimes [8]. It was reported that the coordination number of R(III) ions often decreases along the period due to lanthanide contraction [9]. So far a few examples of rare earth tartrate are known [10]. Thushari et al. [11], Athar et al. [12], Yan et al. [13] and Wang et al. [14] reported the hydrothermal synthesis of lanthanide tartrates with different structures, respectively. Herein we report the synthesis and structural characterization of seven new rare earth MOFs with the general formulas $[R_2(tar)_3(H_2O)_2]_n$ (R=Y (**1**), Sm (**4**), Eu (**5**), Tb (**6**), Dy (**7**)) and $[R_2(tar)_2(C_2O_4)(H_2O)_2]_n \cdot 4nH_2O$ (R=Nd (**2**), La (**3**)). These seven MOFs are all based on the assembly of tartaric acid (H_2tar) with rare earth oxides (R_2O_3) under hydrothermal conditions (Scheme 1). It was found that tar^{2-} ligand not only has versatile traits of coordination chemistry (Scheme 2), but can lead to the novel 3D frameworks and unusual topologies, such as an unusual **fsc**-3,4-*Iba*2 topology and a rare **fsx**-4,5-$P2_1/c$ topology.

2. Experiment section

2.1. Materials and measurements

All chemicals were of analytical reagent grade, commercially purchased and used as supplied. All hydrothermal reactions were performed in the 25 mL Teflon-lined stainless steel Parr bomb. Data

* Corresponding author. Fax: +86 579 82282269.
E-mail addresses: sky37@zjnu.edu.cn, sky37@zjnu.cn (Y.-L. Feng).

0022-4596/$ - see front matter © 2011 Elsevier Inc. All rights reserved.
doi:10.1016/j.jssc.2011.11.012

collection was performed with Mo $K\alpha$ radiation (λ=0.71073 Å) on a Bruker APEX II area-detector diffractometer. Elemental analyses were carried out using a Perkin-Elmer 2400 II elemental analyzer. X-ray powder diffraction (XRPD) intensities were measured at 298 K on a PHILIPS PW3040/60 powder diffractometer with Cu $K\alpha$ radiation (λ=1.5406 Å). IR spectra were measured in KBr pellets on a Nicolet 5DX FT-IR spectrometer. The thermogravimetric measurements were performed on preweighed samples in an oxygen (25%) and nitrogen (75%) mixed stream using a Netzsch STA449C apparatus in the temperature range of 30–800 °C with a heating rate of 5 °C/min. UV–vis spectra of the solid powder materials were measured on a Nicolet Evolution 500 UV–vis spectrophotometer in the range of 200–850 nm, and the excitation and luminescence spectra were performed on a HITACHIF-2500 fluorescence spectrometer in solid state at room temperature.

2.2. Synthesis of $[Y_2(tar)_3(H_2O)_2]_n$ (**1**)

Y_2O_3 (0.5 mmol, 0.1129 g) and H_2tar (1.0 mmol, 0.1501 g) were mixed in 20 mL distilled water. Then the mixture was transferred into a Teflon-lined stainless steel vessel (25 mL) and heated to 160 °C for 72 h. It was cooled to room temperature over 3 day. Colorless crystals of $[Y_2(tar)_3(H_2O)_2]_n$ (**1**) were obtained and collected by filtration, washed with water, then dried in air, 74% yield (based on H_2tar). IR (KBr, cm^{-1}): 3360vs, 3290vs, 2930m, 2890m, 2750w, 2330w, 1580s, 1390vs, 1360vs, 1110s, 818w, 756m, 644m, 571m. Anal. Calc. for $C_{12}H_{16}Y_2O_{20}$: C, 21.90; H, 2.45. Found: C, 21.92; H, 2.50%.

2.3. Synthesis of $[La_2(tar)_2(C_2O_4)(H_2O)_2]_n \cdot 4nH_2O$ (**2**)

A similar hydrothermal synthesis of La_2O_3 (0.5 mmol, 0.1629 g) with H_2tar (1.0 mmol, 0.1982 g) in 20 mL distilled water gave $[La_2(tar)_2(C_2O_4)(H_2O)_2]_n \cdot 4nH_2O$ (**2**) as colorless crystals (35% yield). IR (KBr cm^{-1}): 3420vs, 2920s, 2850m, 2160w, 2010w, 1850m, 1760s, 1600s, 1470m, 1410m, 1380m, 1260s, 1110m, 906m, 714m, 636m, 532m. Anal. Calc. for $C_{10}H_{20}La_2O_{22}$: C, 15.60; H, 2.62. Found: C, 15.63; H, 2.64%.

2.4. Synthesis of $[Nd_2(tar)_2(C_2O_4)(H_2O)_2]_n \cdot 4nH_2O$ (**3**)

A similar hydrothermal synthesis of Nd_2O_3 (0.5 mmol, 0.1682 g) with H_2tar (1.0 mmol, 0.1501 g) in 20 mL distilled water gave $[Nd_2(tar)_2(C_2O_4)(H_2O)_2]_n \cdot 4nH_2O$ (**3**) as colorless crystals (32% yield). IR (KBr, cm^{-1}): 3400vs, 2920s, 2850s, 2460w, 1630m, 1460w, 1380w, 1190w, 1090vs, 918w, 706m, 594. Anal. Calc. for $C_{10}H_{20}Nd_2O_{22}$: C, 15.38; H, 2.58. Found: C, 15.41; H, 2.60%.

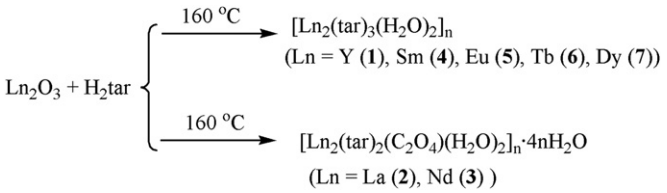

Scheme 1. . Hydrothermal syntheses of **1**–**7**.

2.5. Synthesis of $[Sm_2(tar)_3(H_2O)_2]_n$ (**4**)

A similar hydrothermal reaction of Sm_2O_3 (0.5 mmol, 0.1744 g) with H_2tar (1.0 mmol, 0.1501 g) in 20 mL distilled water gave $[Sm_2(tar)_3(H_2O)_2]_n$ (**4**) as light yellow crystals (74% yield). IR (KBr, cm^{-1}): 3420vs, 2900m, 2820m, 2330w, 1600s, 1450m, 1400m, 1360m, 1310w, 1250w, 1100m, 1030w, 850w, 775m, 572 m. Anal. Calc. for $C_{12}H_{16}Sm_2O_{20}$: C, 18.46; H, 2.07. Found: C, 18.45; H, 2.06%.

2.6. Synthesis of $[Eu_2(tar)_3(H_2O)_2]_n$ (**5**)

A similar hydrothermal reaction of Eu_2O_3 (0.5 mmol, 0.1755 g) with H_2tar (1.0 mmol, 0.1501 g) in 20 mL distilled water gave $[Eu_2(tar)_3(H_2O)_2]_n$ (**5**) as colorless crystals (77% yield). IR (KBr, cm^{-1}): 3430vs, 2920m, 2850m, 2350w, 1620s, 1590s, 1460m, 1420m, 1380m, 1320w, 1260w, 1120m, 1040w, 852w, 775w, 613m. Anal. Calc. for $C_{12}H_{16}Eu_2O_{20}$: C, 18.38; H, 2.06. Found: C, 18.42; H, 2.08%.

2.7. Synthesis of $[Tb_2(tar)_3(H_2O)_2]_n$ (**6**)

A similar hydrothermal reaction of Tb_2O_3 (0.5 mmol, 0.1829 g) with H_2tar (1.0 mmol, 0.1501 g) in 20 mL distilled water gave $[Tb_2(tar)_3(H_2O)_2]_n$ (**6**) as light yellow crystals (70% yield). IR (KBr, cm^{-1}): 3420vs, 2910m, 2850w, 2340w, 2370w, 1600s, 1460m, 1460m, 1380m, 1320w, 1250w, 1120m, 1040w, 849w, 779w, 594m. Anal. Calc. for $C_{12}H_{16}Tb_2O_{20}$: C, 18.06; H, 2.02. Found: C, 18.09; H, 2.04%.

2.8. Synthesis of $[Dy_2(tar)_3(H_2O)_2]_n$ (**7**)

A similar hydrothermal reaction of Dy_2O_3 (0.5 mmol, 0.1865 g) with H_2tar (1.0 mmol, 0.1501 g) in 20 mL distilled water gave $[Dy_2(tar)_3(H_2O)_2]_n$ (**7**) as colorless crystals (74% yield). IR (KBr cm^{-1}): 3430vs, 2920m, 2850m, 2360w, 1590s, 1460m, 1380m, 1320m, 1260m, 1120m, 1040m, 922w, 856w, 779w, 598m. Anal. Calc. for $C_{12}H_{16}Dy_2O_{20}$: C, 17.90; H, 2.00. Found: C, 17.92; H, 2.03%.

2.9. Single-crystal structure determination

The diffraction data for MOFs **2**, **3**, **5** and **7** were collected on a Bruker APEX II diffractometer equipped with a graphite–monochromatized Mo–$K\alpha$ radiation (λ=0.71073 Å) at 296(2) K. Data intensity was corrected by Lorentz-polarization factors and empirical absorption. The structures were solved by direct methods and expanded with difference Fourier techniques. All non-hydrogen atoms were refined anisotropically. Except the

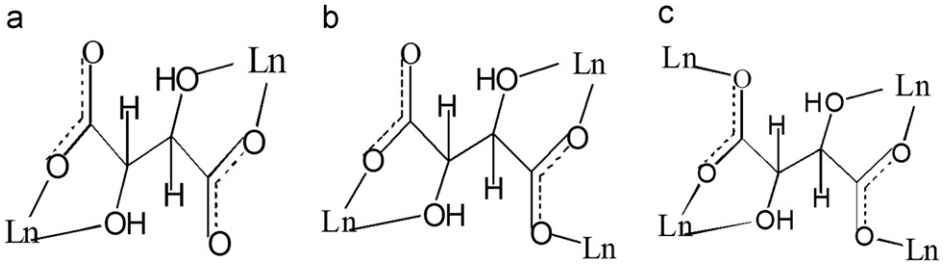

Scheme 2. . Binding modes of tar^{2-} found in the title MOFs, (a) μ_2, κ^4, (b) μ_3, κ^5, (c) μ_4, κ^6.

Table 1
Crystal data and structure refinement for **2**, **3**, **5** and **7**.

Complex	**2**	**3**	**5**	**7**
Empirical formula	$C_{10}H_{20}La_2O_{22}$	$C_{10}H_{20}Nd_2O_{22}$	$C_{12}H_{16}Eu_2O_{20}$	$C_{12}H_{16}Dy_2O_{20}$
Formula weight	770.08	780.74	784.17	805.25
Crystal system	monoclinic	monoclinic	orthorhombic	orthorhombic
Space group	$P2_1/c$	$P2_1/c$	*Iba*2	*Iba*2
a (Å)	6.1092(2)	6.0528(2)	12.5257(2)	12.4764(1)
b (Å)	7.6866(2)	7.6177(3)	14.2085(1)	14.1541(2)
c (Å)	22.6987(6)	22.3364(8)	10.5397(1)	10.4935(1)
β (deg.)	91.657(1)	91.412(2)		
V (Å^3)	1065.46(5)	1029.58(6)	1875.77(4)	1853.07(3)
Z	2	2	4	4
D_c	2.400	2.518	2.777	2.886
μ (mm^{-1})	4.063	5.098	6.738	8.116
F (0 0 0)	740	752	1496	1520
θ_{min}, θ_{max} (deg.)	1.80, 27.61	1.80, 27.49	2.87, 27.42	2.18, 27.51
Reflections Collected	14265	11815	13815	7719
Unique reflections (R_{int})	2443 (0.0200)	2253 (0.0244)	1131 (0.0402)	1126 (0.0262)
Observed Reflections ($I > 2\sigma(I)$)	2263	2147	1107	1083
Parameters refined	196	208	171	171
S on F^2	1.025	1.000	1.001	1.054
R, wR ($I > 2\sigma(I)$)	0.0191, 0.0525	0.0417, 0.0933	0.0161, 0.0454	0.0178, 0.0478
R, wR (all data)	0.0213, 0.0541	0.0438, 0.0942	0.0164, 0.0457	0.0183, 0.0483

$R=[\Sigma|F_o|-|F_c|]/[\Sigma F_o|]$. $wR=\{[\Sigma w(F_o^2-F_c^2)^2]/[\Sigma w(F_o^2)^2]\}^{1/2}$.

Table 2
Selected bond lengths (Å) and angles (deg.) for **2**.

Bond	Distance	Bond	Distance
La1–O5#1	2.490(3)	La1–O1W	2.584(2)
La1–O6#2	2.493(7)	La1–O4#1	2.585(4)
La1–O1	2.506(6)	La1–O8#4	2.601(5)
La1–O7	2.553(7)	La1–O3	2.657(7)
La1–O2#3	2.561(6)		
Angle	(deg.)	Angle	(deg.)
O5#1–La1–O6#2	126.50(6)	O1W–La1–O4#1	144.17(7)
O5#1–La1–O1	73.25(7)	O5#1–La1–O8#4	107.20(7)
O6#2–La1–O1	74.75(7)	O6#2–La1–O8#4	71.85(6)
O5#1–La1–O7	76.05(7)	O1–La1–O8#4	137.51(6)
O6#2–La1–O7	133.73(6)	O7–La1–O8#4	62.40(6)
O1–La1–O7	147.67(7)	O2#3–La1–O8#4	131.40(6)
O5#1–La1–O2#3	70.42(7)	O1W–La1–O8#4	75.71(7)
O6#2–La1–O2#3	149.89(6)	O4#1–La1–O8#4	72.64(6)
O1–La1–O2#3	89.76(6)	O5#1–La1–O3	121.10(6)
O7–La1–O2#3	70.44(6)	O6#2–La1–O3	75.04(6)
O5#1–La1–O1W	147.63(7)	O1–La1–O3	60.44(5)
O6#2–La1–O1W	85.51(7)	O7–La1–O3	132.30(6)
O1–La1–O1W	126.93(7)	O2#3–La1–O3	74.86(6)
O7–La1–O1W	77.34(7)	O1W–La1–O3	67.02(6)
O2#3–La1–O1W	83.53(7)	O4#1–La1–O3	125.60(5)
O5#1–La1–O4#1	60.59(6)	O8#4–La1–O3	131.34(6)
O6#2–La1–O4#1	69.07(6)	O7–La1–O4#1	101.90(6)
O1–La1–O4#1	71.37(6)	O2#3–La1–O4#1	130.62(6)

Symmetry codes: (#1) 1–x, 0.5+y, 0.5–z; (#2) 2–x, 0.5+y, 0.5–z; (#3) 1–x, –0.5+y, 0.5–z; (#4) 1–x, 1–y, –z.

Table 3
Selected bond lengths (Å) and angles (deg.) for **3**.

Bond	Distance	Bond	Distance
Nd1–O5#1	2.438(5)	Nd1–O1W	2.517(6)
Nd1–O6#2	2.444(5)	Nd1–O4#1	2.523(5)
Nd1–O1	2.451(5)	Nd1–O8#4	2.554(6)
Nd1–O7	2.497(5)	Nd1–O3	2.608(5)
Nd1–O2#3	2.499(5)		
Angle	(deg.)	Angle	(deg.)
O5#1–Nd1–O6#2	127.88(17)	O6#2–Nd1–O4#1	69.21(17)
O5#1–Nd1–O1	73.40(19)	O1–Nd1–O4#1	71.30(17)
O6#2–Nd1–O1	75.42(19)	O7–Nd1–O4#1	102.18(18)
O5#1–Nd1–O7	75.0(2)	O2#3–Nd1–O4#1	131.80(19)
O6#2–Nd1–O7	134.11(19)	O1W–Nd1–O4#1	143.7(2)
O1–Nd1–O7	146.8(2)	O5#1–Nd1–O8#4	107.5(2)
O5#1–Nd1–O2#3	70.59(18)	O6#2–Nd1–O8#4	71.05(18)
O6#2–Nd1–O2#3	148.85(18)	O1–Nd1–O8#4	136.97(18)
O1–Nd1–O2#3	89.50(18)	O7–Nd1–O8#4	63.65(17)
O7–Nd1–O2#3	70.40(17)	O2#3–Nd1–O8#4	132.34(17)
O5#1–Nd1–O1W	146.80(18)	O1W–Nd1–O8#4	75.7(2)
O6#2–Nd1–O1W	84.93(19)	O4#1–Nd1–O8#4	72.07(18)
O1–Nd1–O1W	127.37(18)	O5#1–Nd1–O3	122.04(18)
O7–Nd1–O1W	77.5(2)	O6#2–Nd1–O3	74.32(17)
O2#3–Nd1–O1W	82.9(2)	O1–Nd1–O3	61.40(16)
O5#1–Nd1–O4#1	61.72(17)	O7–Nd1–O3	131.97(17)
O4#1–Nd1–O3	125.71(16)	O2#3–Nd1–O3	74.54(16)
O8#4–Nd1–O3	130.14(18)	O1W–Nd1–O3	66.41(18)

Symmetry codes: (#1) 1–x, 0.5+y, 0.5–z; (#2) 2–x, 0.5+y, 0.5–z; (#3) 1–x, –0.5+y, 0.5–z; (#4) 1–x, 1–y, –z.

hydrogen atoms on oxygen atoms were located from the difference Fourier maps, the other hydrogen atoms were generated geometrically. The two lattice water molecules of MOFs **2** and **3** in an asymmetry unit are disordered and the occupancies of MOF **2** refined to the same of 0.70:0.30, while the occupancies of MOF **3** refined to 0.70:0.30 and 0.57:0.43, respectively. All calculations were performed using SHELXS-97 and SHELXL-97 [15]. Basic information pertaining to crystal parameters and structure refinement are summarized in Table 1, and the selected bond lengths and bond angles are listed in Tables 2–5. CCDC 694077, 694076, 694078 and 684819 contain the Supplementary crystallographic data for MOFs **2**, **3**, **5** and **7**, respectively.

3. Results and discussion

3.1. Syntheses

It was reported that tartaric acid can endure hydrothermal conditions up to 160 °C to form the robust, open-framework [11]. Our synthetic strategy for the *R*(III) MOFs is depicted in Scheme 1. Single crystals of MOFs **2**, **3**, **5** and **7** were obtained, whereas MOFs **1**, **4**, **6** only gained power samples. As shown in Figs. 1 and 2, all XRPD patterns measured for the as-synthesized samples are in agreement with the results simulated from the single-crystal X-ray data, indicating that the crystal structures are representative of the bulk

Table 4
Selected bond lengths (Å) and angles (deg.) for **5**.

Bond	Distance	Bond	Distance
Eu1–O5#1	2.328(2)	Eu1–O8	2.395(3)
Eu1–O1W	2.326(5)	Eu1–O7	2.423(3)
Eu1–O1	2.369(7)	Eu1–O4#1	2.444(5)
Eu1–O2#2	2.373(2)	Eu1–O3#2	2.478(3)
Angle	(deg.)	Angle	(deg.)
O5#1–Eu1–O1W	79.65(10)	O8–Eu1–O7	64.88(7)
O5#1–Eu1–O1	76.32(8)	O5#1–Eu1–O4#1	65.39(11)
O1W–Eu1–O1	85.18(12)	O1W–Eu1–O4#1	143.79(9)
O5#1–Eu1–O2#2	77.19(9)	O1–Eu1–O4#1	77.93(12)
O1W–Eu1–O2#2	98.16(12)	O2#2–Eu1–O4#1	83.61(13)
O1–Eu1–O2#2	152.22(13)	O8–Eu1–O4#1	124.28(11)
O5#1–Eu1–O8	143.68(11)	O7–Eu1–O4#1	72.76(13)
O1W–Eu1–O8	79.22(14)	O5#1–Eu1–O3#2	132.23(9)
O1–Eu1–O8	72.76(8)	O1W–Eu1–O3#2	78.58(14)
O2#2–Eu1–O8	135.00(11)	O1–Eu1–O3#2	142.33(15)
O5#1–Eu1–O7	138.1(2)	O2#2–Eu1–O3#2	64.63(7)
O1W–Eu1–O7	141.57(16)	O8–Eu1–O3#2	70.93(10)
O1–Eu1–O7	96.34(10)	O7–Eu1–O3#2	77.15(8)
O2#2–Eu1–O7	97.79(12)	O4#1–Eu1–O3#2	132.24(13)

Symmetry codes: (#1) 2–*x*, *y*, 0.5+*z*; (#2) 0.5+*x*, 1.5–*y*, *z*.

Table 5
Selected bond lengths (Å) and angles (deg.) for **7**.

Bond	Distance	Bond	Distance
Dy1–O5#1	2.302(3)	Dy1–O8	2.382(4)
Dy1–O1W	2.311(5)	Dy1–O7	2.384(3)
Dy1–O1	2.343(2)	Dy1–O4#1	2.398(6)
Dy1–O2#2	2.344(3)	Dy1–O3#2	2.467(3)
Angle	(deg.)	Angle	(deg.)
O5#1–Dy1–O1W	78.66(11)	O8–Dy1–O7	65.57(8)
O5#1–Dy1–O1	76.58(9)	O5#1–Dy1–O4#1	66.26(13)
O1W–Dy1–O1	85.88(14)	O1W–Dy1–O4#1	143.94(10)
O5#1–Dy1–O2#2	77.41(10)	O1–Dy1–O4#1	78.39(14)
O1W–Dy1–O2#2	97.43(14)	O2#2–Dy1–O4#1	83.32(15)
O1–Dy1–O2#2	152.57(15)	O8–Dy1–O4#1	125.09(13)
O5#1–Dy1–O8	142.82(13)	O7–Dy1–O4#1	73.14(15)
O1W–Dy1–O8	79.01(17)	O5#1–Dy1–O3#2	131.71(11)
O1–Dy1–O8	72.51(9)	O1W–Dy1–O3#1	77.23(16)
O2#2–Dy1–O8	134.90(12)	O1–Dy1–O3#2	141.38(18)
O5#1–Dy1–O7	139.4(2)	O2#2–Dy1–O3#2	65.14(8)
O1W–Dy1–O7	141.54(18)	O8–Dy1–O3#2	70.32(12)
O1–Dy1–O7	96.81(11)	O7–Dy1–O3#2	77.13(9)
O2#2–Dy1–O7	97.23(13)	O4#1–Dy1–O3#2	132.97(15)

Symmetry codes: (#1) –*x*, *y*, –0.5+*z*; (#2) –0.5+*x*, 0.5–*y*, *z*.

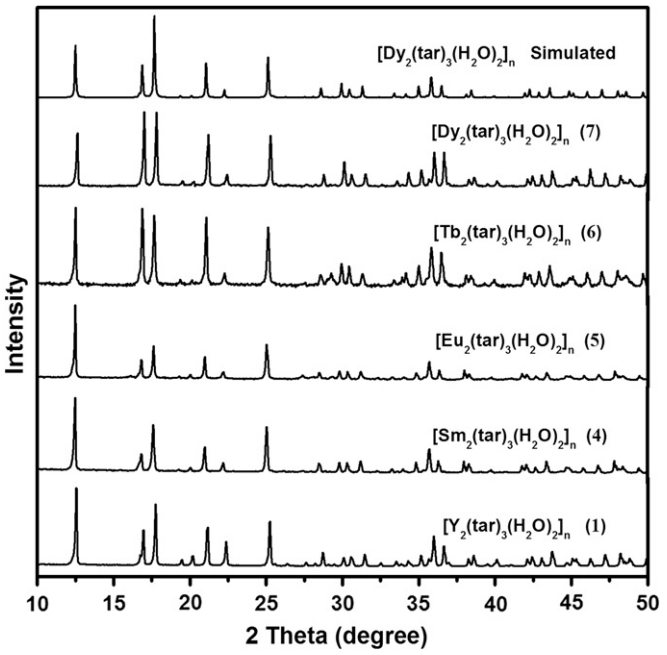

Fig. 1. Powder X-ray diffraction pattern of MOFs **1**, **4**, **5**, **6** and **7** compared with the simulated pattern.

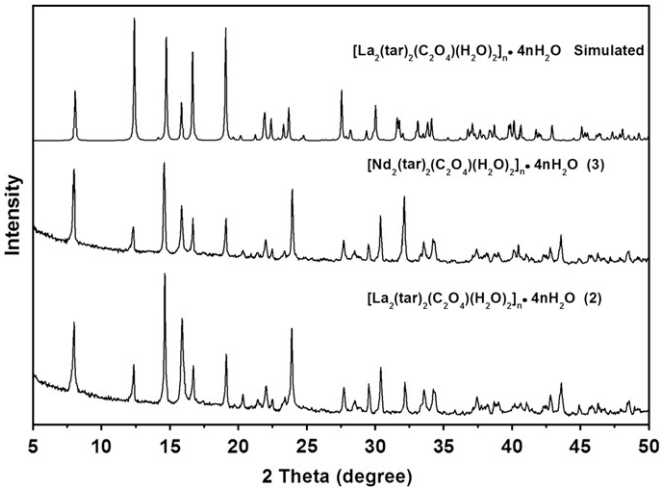

Fig. 2. Powder X-ray diffraction pattern of MOFs **2** and **3** compared with the simulated pattern.

materials. The differences in intensity are perhaps due to the preferred orientation of the powder samples. Therefore these five MOFs $[R_2(tar)_3(H_2O)_2]_n$ (R=Y (**1**), Sm (**4**), Eu (**5**), Tb (**6**), Dy (**7**)) would have similar structures, which were obtained from the reaction of R_2O_3 with H_2tar at a temperature of 160 °C. However, we obtained another type of MOFs $[R_2(tar)_2(C_2O_4)(H_2O)_2]_n \cdot 4nH_2O$ (R=La (**2**), Nd (**3**)) following similar strategy, which indicated that there should be in situ formation of $C_2O_4^{2-}$ during hydrothermal syntheses (Scheme 1). The same results were obtained when we used $R(NO_3)_2$ instead of R_2O_3 in the hydrothermal reactions. Formation of oxalic acid from tartaric acid oxidation has been known for long [16]. In general, to transform H_2tar into $C_2O_4^{2-}$, there should be other reagents such as strong oxidizers like H_2SO_4 participating in the reaction. However, in our reported reaction there is no other oxidizer. We supposed the mechanism as follow: compared with the radius of Sm, Eu, Tb and Dy, the one of La, Nd is shorter as lanthanide contraction, consequently enhancing oxidability of La, Nd. It is thus possible that the metal plays a role in the oxidation reaction and results in the oxidative cleavage of the acid and in situ formation of oxalic acid.

3.2. Crystal structures of *5* and *7*

The single-crystal X-ray diffraction analyses revealed that **5** and **7** are isomorphous structures. The similar MOFs $[R_2(L\text{-}tar)_3(H_2O)_2] \cdot 3H_2O$ (R=Y, La–Yb) in triclinic system with space group *P*-1 have been reported by Thushari et al. [11], in which the *R* ions have 9-coordinate environments. The title crystals crystallize in orthorhombic system with space group *Iba*2. Therefore, only the structure of **5** is described here in detail. As shown in Fig. 3, The Dy(III) center is eight-coordinated by one coordinated aqua molecule and seven oxygen atoms from four carboxyl groups and three α-hydroxyl groups of four tar^{2-} ligands to give a distorted dodecahedron geometry. The Dy–O distances range from 2.302(3) to 2.467(3) Å, these values are similar to those found for DyO_8 dodecahedron [17]. The O–Dy–O angles lie in the

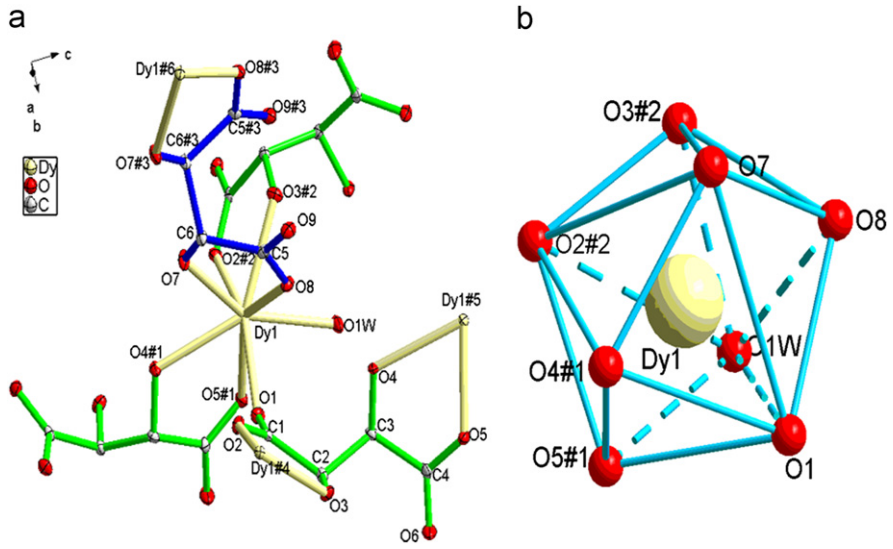

Fig. 3. (a) Coordination environment of Dy(III) in **5** showing the atom labeling, thermal ellipsoids are shown at the 30% probability level. All H atoms molecules are omitted for clarity. (b) The distorted dodecahedron of the Dy(III) ion of **5**. Symmetry codes: (#1) $-x$, y, $-0.5+z$; (#2) $-0.5+x$, $0.5-y$, z; (#3) $-x$, $-y$, z; (#4) $0.5+x$, $0.5-y$, z; (#5) $-x$, y, $0.5+z$; (#6) $-x$, $-y$, z.

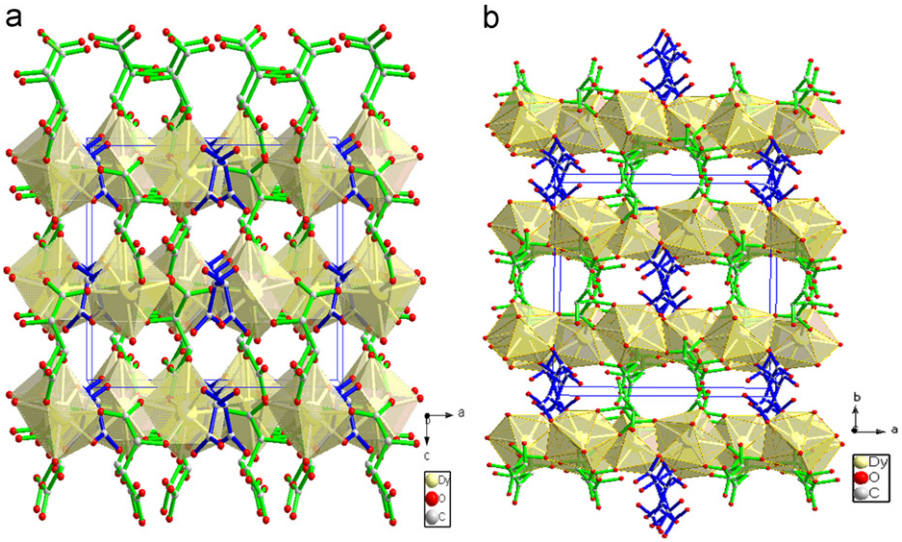

Fig. 4. 3D network of **5** showing the cell edges down (a) *b* axis and (b) *c* axis.

range of 65.14(8)–152.57(15)°, which are close to those in the previously reported Dy(III) MOFs [18]. In this framework, there are two kinds of tar^{2-} ligands which display different binding fashions. One tar^{2-} ligand adopts the μ_2, κ^4 coordination mode and bridges two Dy(III) cations along *b* axis using two monodentate carboxyl groups and two α-hydroxyl groups (Scheme 2a); the other one acts as the μ_3, κ^5 coordination mode and bridges three Dy(III) cations using one monodentate carboxyl group, one bidentate carboxyl group and two α-hydroxyl groups (Scheme 2b). As shown in Fig. 4, the tar^{2-} ligands in the μ_3, κ^5 coordination mode combine with the Dy(III) ions to form a condensed 2D slab in the *ac* plane, while the tar^{2-} ligands in the μ_2, κ^4 coordination mode interlink the neighboring slabs to generate the 3D framework.

Better insight of this 3D architecture can be achieved by topology analysis. As shown in Fig. 5, each Dy(III) ion is linked to four tar^{2-} ligands to represent a 4-connected node (Fig. 5a), meanwhile the two independent tar^{2-} ligands act as 3- and 2-connected nodes (Fig. 5b, c), respectively, resulting in an unusual non-interpenetrating (3,4)-connected **fsc**-3,4-*Iba2* topology with Schläfli symbol of $(6^3)(6^5.8)$, the vertex symbol using TOPOS 4.0 [19] calculation gives $(6.6.6_2)$ for the 3-connected node and (6.6.6.6.6.8) for the 4-connected node, and is thus corresponding to the topology of **fsc**-3,4-*Iba*2 (Fig. 5d). Topology **fsc**-3.4-*Iba*2 is derived from (4,6)-connect **fsc** net, the maximal symmetry of this unique net is *Iba*2. To date, only these type of MOFs [11] display this unusual topology.

3.3. Crystal structures of **2** and **3**

2 and **3** are isomorphous structures and crystallize in the monoclinic $P2_1/c$ space group. Take **2** as a representation, the La(III) center is nine-coordinated by one aqua molecule, two oxygen atoms from one oxalate anion ($C_2O_4^{2-}$) and six oxygen atoms from four carboxyl groups and two α-hydroxyl groups of four tar^{2-} ligands, as illustrated in Fig. 6. The geometry of the center can be best described as a distorted tricapped trigonal prism with O3, O5#1 and O8#4 atoms in the capped positions. The La–O bond lengths are in the range of 2.490(3)–2.657(7) Å, and the O–La–O angles lie in the range of 60.59(6)–149.89(6)°,

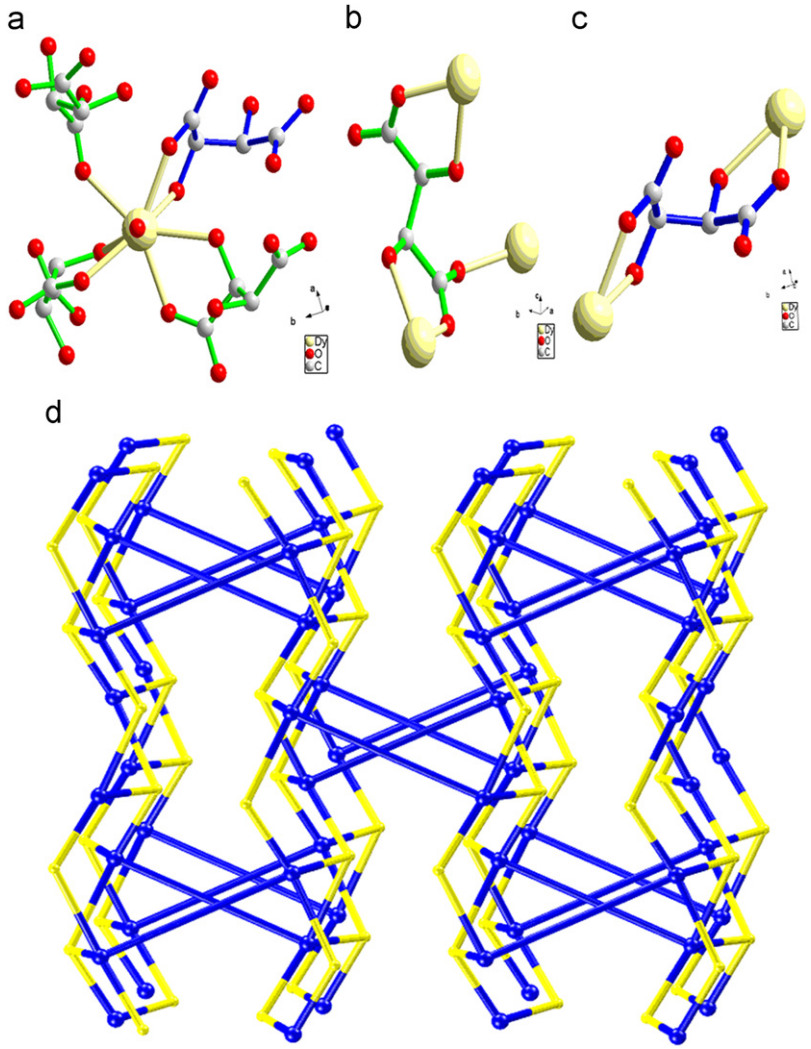

Fig. 5. (a) 4-connected Dy(III) unit coordinated with four tar^{2-} units; (b) 3-connected tar^{2-} unit linked with three Dy(III) units; (c) 2-connected tar^{2-} unit connected with two Dy(III) units; and (d) schematic representation of the **fsc**-3,4-*Iba*2 topology of **5**.

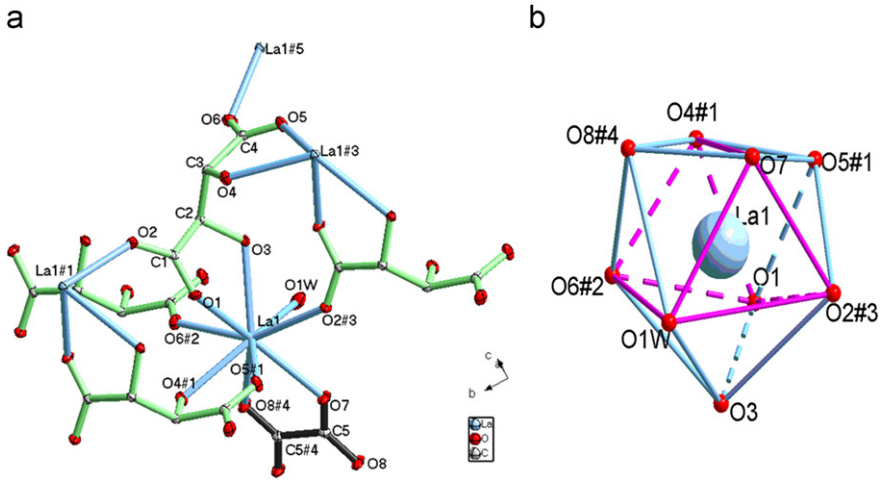

Fig. 6. A(a) Coordination environment of La(III) in **2** showing the atom labeling, thermal ellipsoids are shown at the 30% probability level. All H atoms are omitted for clarity. (b) The distorted tricapped trigonal prism coordination polyhedron of the La(III) ion of **2**. Symmetry codes: (#1) 1–*x*, 0.5+*y*, 0.5–*z*; (#2) 2–*x*, 0.5+*y*, 0.5–*z*; (#3) 1–*x*, –0.5+*y*, 0.5–*z*; (#4) 1–*x*, 1–*y*, –*z*; (#5) 2–*x*, –0.5+*y*, 0.5–*z*.

which are comparable to those in the previously reported lanthanum MOFs [20]. The tar^{2-} ligand can be classed as μ_4, κ^6 (Scheme 2c), and binds to four La(III) ions through six oxygen atoms from four bidentate carboxyl groups, and two α-hydroxyl groups, forming a 2D layer in the *ab* plane; compared with the tar^{2-} ligand in the MOFs $[La(tar)_{1.5}(H_2O)]\cdot H_2O$ [14], the $C_2O_4^{2-}$

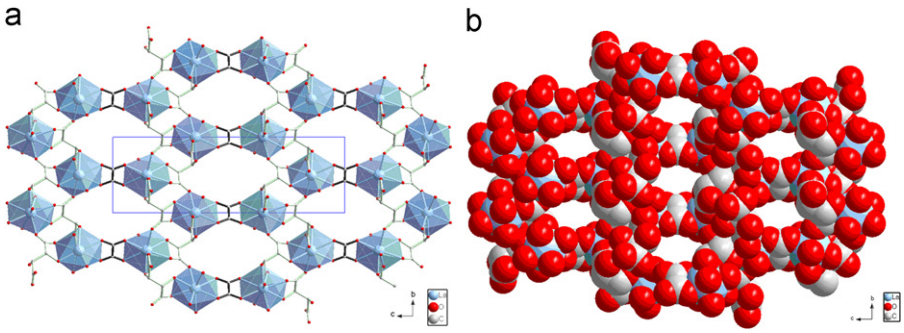

Fig. 7. (a) Polyhedral representation and (b) space-filling model of 2 framework viewed down a axis. All H atoms and lattice water molecules are omitted for clarity.

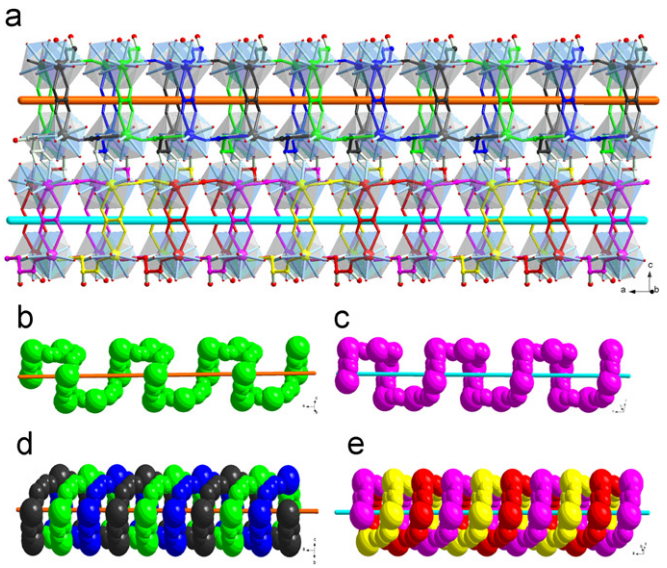

Fig. 8. (a) Polyhedral representation of **2** framework viewed along *a* axis showing right- and left-handed helixes; (b) space-filling model of right-handed single helical chain; (c) space-filling model of left-handed single helical chain; (d) space-filling model of right-handed triple helical chains; and (e) space-filling model of left-handed triple helical chains.

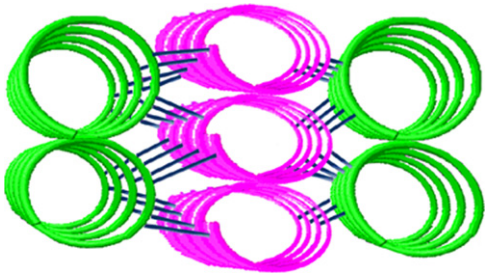

Fig. 9. Schematic illustration of the 3D network of **2**, pink helixes represent left handed triple helical chains, green helixes represent right handed triple helical chains. (For interpretation of the references to colour in this figure legend, the reader is referred to the web version of this article.)

anion also acts as a μ_2-bridge ligand and interconnects the neighboring layers, constructing a 3D network with hydrophilic channels of *ca.* 6.64 × 7.69 Å dimension along *a* axis (Fig. 7). As shown in Fig. 8, it is remarkable that the hydrophilic channels are bounded by triple helical chains along *a* axis, each triple helical chain is interwoven by three similar single helical chains ($La–C_2O_4^{2-}–La–COO^-–La–tar^{2-}–La–C_2O_4^{2-}–La–COO^-–La–tar^{2-}–La$) with 2_1 screw axis and a pitch of 18.3276 Å. These triple helical chains are alternately arranged in a right- and left-handed sequence, as illustrated in Fig. 9, so that the whole 3D structure

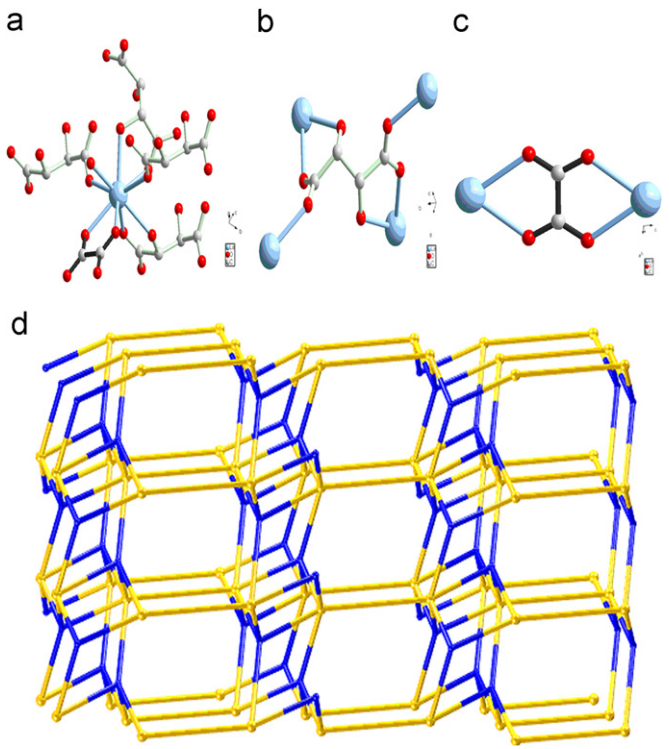

Fig. 10. (a) 5-connected La(III) unit coordinated with four tar^{2-} units and one $C_2O_4^{2-}$ unit; (b) 4-connected tar^{2-} unit linked with four La(III) units. (c) 2-connected $C_2O_4^{2-}$ unit connected with two La(III) units. (d) Schematic representation of the **fsx**-4,5-$P2_1/c$ topology of **2**.

does not show chirality. Additionally, eight lattice water molecules per unit cell occupy these hydrophilic channels, to provide multiple intermolecular hydrogen bonds among lattice waters and the hydrophilic channels to stabilize the crystal structure.

As shown in Fig. 10, each tar^{2-} ligand is linked to four La(III) cations to represent a 4-connected node (Fig. 10a), each $C_2O_4^{2-}$ anion acts as 2-connected node by connecting to two La(III) cations (Fig. 10b) and each La(III) cation serves for a 5-connected node by combining four tar^{2-} ligands and one $C_2O_4^{2-}$ anion (Fig. 10c). Hence, a binodal **fsx**-4,5-$P2_1/c$ topology network is formed with Schläfli symbol of $(4^2.6^4)(4^2.6^7.8)$ (Fig. 10d), the vertex symbol using TOPOS 4.0 [19] calculation gives $(4.6_2.4.6_4.6_4.6_4)$ for the 4-connected node and $(4.4.6.6_2.6_2.6_2.6_3.6_3.6_4.8_{10})$ for the 5-connected node, and is thus corresponding to the topology type with transformation symbol [19a,19e] **fsx**/*I*4/*mmm*–P$2_1/c$ (**-a, b, a**+**c**); Bond sets: **1,3,4,5,6**:**fsx**. This symbol means that the net is derived from the binodal net **fsx** by decreasing its space-group symmetry from *I*4/*mmm* to $P2_1/c$ with transformation of the unit cell by (−**a, b, a**+**c**) vector, and

breaking all non-equivalent edges in the resulting net except the edges No 1, 3, 4, 5 and 6. In the TTD collection, there are 85 binodal nets derived from (5,6)-connected **fsx** net, only 10 of them was found in real structures to date, such as: **fsx**-3,4-*C*2/*c*-1; **fsx**-3,4-*C*2/*c*-2; **fsx**-3,4-*Fd*-3m; **fsx**-3,4-*Pccn*; **fsx**-4,5-*C*2/*c*; **fsx**-4,5-*C*2/*c*; **fsx**-4,5-*Cmce*-1; **fsx**-4,5-*Cmce*-2; **fsx**-4,5-$P2_12_12$; **fsx**-4,5-$P6_3/mmc$, **fsx**-4,5-*R*-3*m*. As the $C_2O_4^{2-}$ anion and the above-mentioned tar^{2-} ligand also acts as a 2-connected node, topology network of **2** or **3** is the same as reported MOFs $[La(tar)_{1.5}(H_2O)]\cdot H_2O$ [14]. To the best of our knowledge, there is only one known $[La(tar)_{1.5}(H_2O)]\cdot H_2O$ crystal structure about topology **fsx**-4.5-$P2_1/c$ in any compilations and databases[19,21].

3.4. UV–vis spectroscopy

The UV–vis spectra of the solid powder materials were measured at room temperature. As shown in the Fig. 11, there are strong absorption bands in UV spectral range (201–229 nm (**1**), 201–223 nm (**2**), 201–225 nm (**3**), 201–240 nm (**4**), 201–255 nm (**5**), 204–222 nm (**6**), 201–221 nm (**7**)) which come from the carbonyl groups of tar^{2-} and $C_2O_4^{2-}$. **1** and **2** reveals no significant absorption peaks from 300 to 850 nm (Fig. 11a, b), which is partly because La(III) and Y(III) are closed shell structure, there is no electronic in the *f*-orbital, and the electronic transitions from ground state to excited multiplets demands higher energy. **3** reveals strong absorption peaks around 330, 356, 429, 462, 475, 513, 524, 580, 626, 680, 746 and 799 nm (Fig. 11c), which correspond to the $f\rightarrow f$ electronic transitions from the $^4I_{9/2}$ ground state of Nd(III) to the different excited multiplets [22]. **4** reveals absorption peaks around 317, 345, 364, 375, 403, 419, 438, 464 and 477 nm (Fig. 11d), which correspond to the $f\rightarrow f$ electronic transitions from the $^6H_{5/2}$ ground state of Sm(III) to the different excited multiplets [23]. **5** reveals several absorption peaks around 364, 379, 395, 419 and 465 nm (Fig. 11e); which would correspond to the $f\rightarrow f$ electronic transitions from the $^7F_0$ ground state, the $^7F_1$ first excited state or the $^7F_2$ second excited state of Eu(III) to the higher excited multiplets [24]. **6** reveals a significant absorption band between 235 and 400 nm (Fig. 11f), which correspond to the $f\rightarrow f$ electronic transitions from the $^7F_6$ ground state of Tb(III) to the different excited multiplets [25]. **7** reveals significant peaks around 326, 338, 352, 366, 389, 428, 452, 473, 755, 764, 805 and 819 nm (Fig. 11g), which may arise from the $f\rightarrow f$ electronic transitions from the $^6H_{15/2}$ ground state of Dy (III) to the different excited multiplets [26].

3.5. Luminescence properties

The solid-state luminescence properties of MOFs **3**, **4**, **5**, **6** and **7** were investigated at room temperature. These MOFs exhibit corresponding characteristic luminescence at the excitation of 600, 401, 383, 361 and 364 nm, respectively. Fig. 12a shows the characteristic emission of **3**, the peaks at 822, 827, 834 and 840 nm would correspond to the transition of Nd(III) ions from $^4F_{5/2}\rightarrow{}^4I_{9/2}$ or $^2H_{9/2}\rightarrow{}^4I_{9/2}$, and the peak at 880 nm is assigned to the transition of Nd(III) ions from $^4F_{3/2}\rightarrow{}^4I_{9/2}$ [27]. **4** emits strong pink emission luminescence (Fig. 12b) and exhibits characteristic peaks at 547, 562, 565, 597, 602, 605, 616, 621, 636, 643, 651, 659 nm due to the transitions of Sm(III) ions from $^4G_{5/2}\rightarrow{}^6H_J$ (J=5/2, 7/2, 9/2, 11/2); the most intense peak is the hypersensitive transition $^4G_{5/2}\rightarrow{}^6H_{9/2}$ at 597 nm [28]. **5** emits intense red luminescence (Fig. 12c) and exhibits characteristic peaks at 579, 588, 592, 596, 611, 616, 621, 650, 687, 689, 607 and 703 nm, corresponding to the transitions of Eu(III) from $^5D_0\rightarrow{}^7F_J$ (J=1, 2, 3, and 4) [29]. Excitation of **6** reveals the expected $^5D_4\rightarrow{}^7F_J$ transitions with J=6, 5, 4, 3 as shown in Fig. 12d, the peaks at 488, 491 and 497 nm would correspond to the transition of Tb(III) ions from $^5D_4\rightarrow{}^7F_6$; the peaks at 542 and 546 nm would correspond to the transition of Tb(III) ions from $^5D_4\rightarrow{}^7F_5$; the peaks at 585 and 588 would correspond to the transition of Tb(III) ions from $^5D_4\rightarrow{}^7F_4$; the peaks at 616 and 621 nm would correspond to the transition of Tb(III) ions from $^5D_4\rightarrow{}^7F_3$ [30]. The characteristic emission of Dy(III) ion in **7** are shown in Fig. 12e. Two strong peaks at 484, 573 nm and a weak peak at 658 nm are assigned to

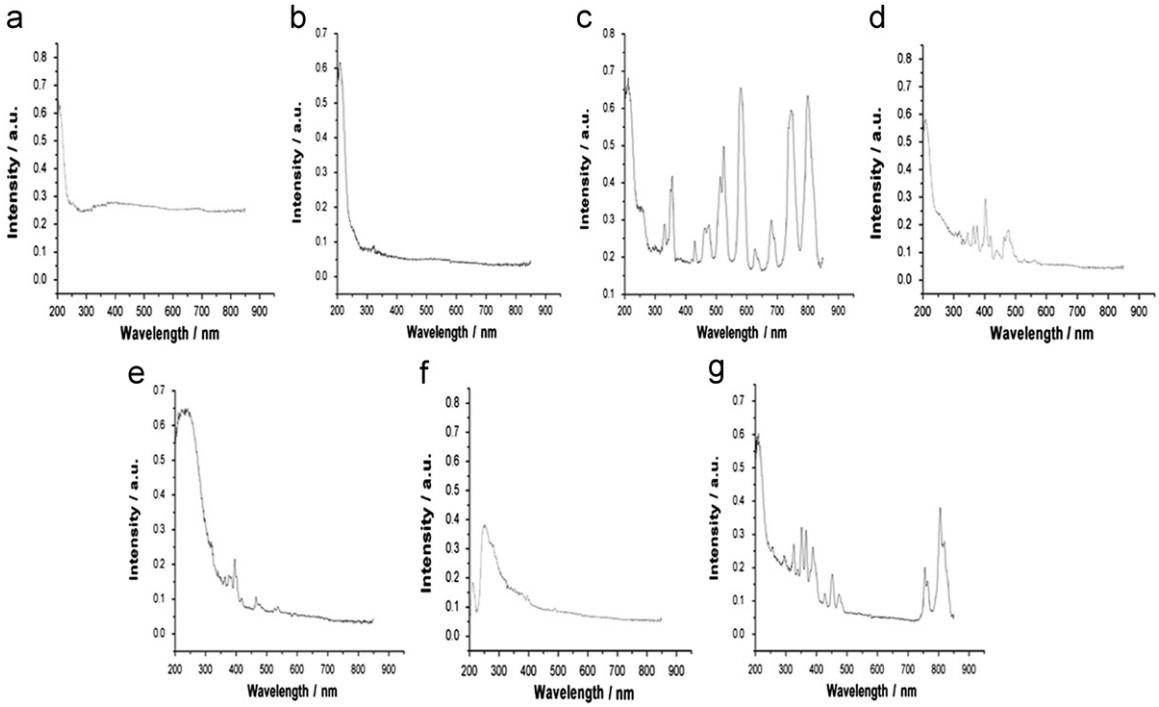

Fig. 11. UV–vis spectra of **1** (a), **2** (b), **3** (c) **4** (d) **5** (e) **6** (f) **7** (g) in solid state.

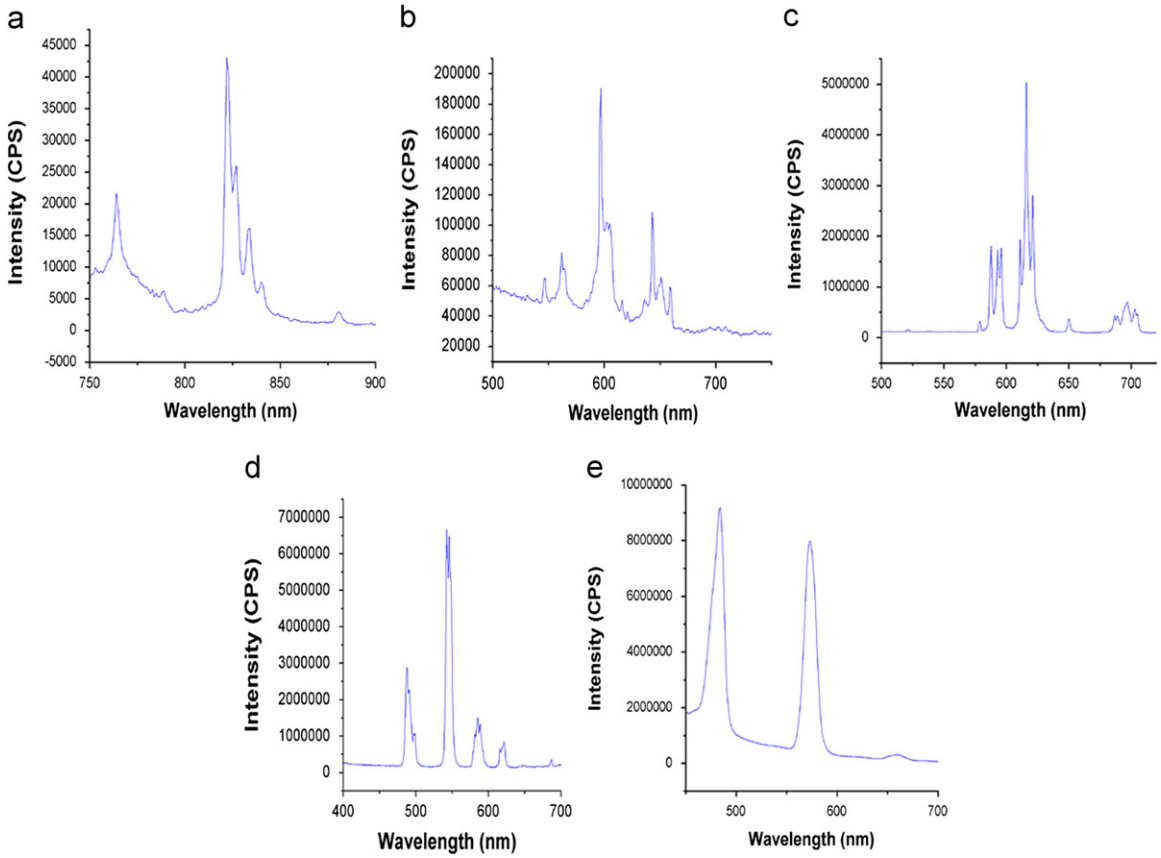

Fig. 12. Emission spectra of (a) **3,** (b) **4**, (c) **5,** (d) **6,** (e) **7** in solid state excited at 600, 401, 383, 361 and 364 nm, respectively.

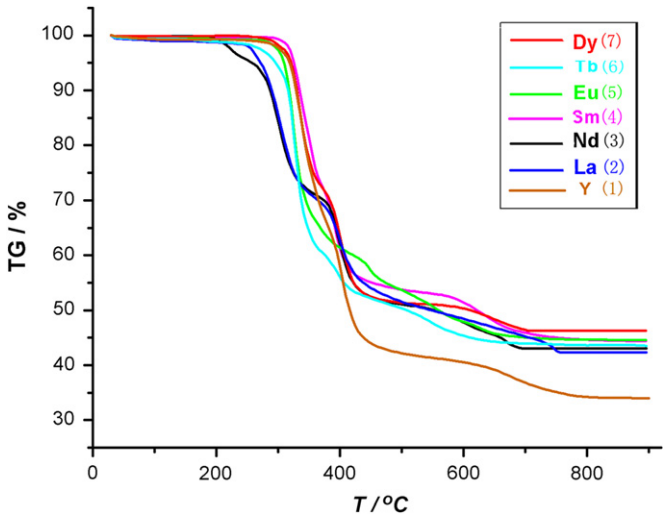

Fig. 13. TG curves of MOFs **1–7**.

the transition of $^4F_{9/2}\rightarrow{}^6H_{15/2}$, $^4F_{9/2}\rightarrow{}^6H_{13/2}$, and $^4F_{9/2}\rightarrow{}^6H_{11/2}$, respectively [31].

3.6. Thermalgravimetric analyses

As shown in Fig. 13, The TG curve exhibits **1** begins to lose weight at 234 °C, all the organic groups and coordinated waters are burned out after 829 °C, the final residuals may be Y_2O_3, the observed total weight loss of 66.03% is compared to the calculated one of 65.69%. **2** and **3** exhibit similar thermal behavior. The TG curves exhibit that **2** begins to lose weight at 180 °C, all the organic groups and waters are burned out after 755 °C, the observed total weight loss of 57.72% is close to the calculated one of 57.69% and the final residuals may be La_2O_3; and **3** begins to lose weight at 200 °C and all the organic groups and waters are burned out after 706 °C, the observed total weight loss of 57.09% is close to the calculated one of 56.90% and the final residuals may be Nd_2O_3. **4**, **5, 6** and **7** also exhibit similar thermal behavior. Their TG curves exhibit that **4** begins to lose weight at 275 °C, all the organic groups and coordinated waters are burned out after 870 °C. The final residuals may be Sm_2O_3; the observed total weight loss of 55.59% is compared to the calculated one of 55.34%; **5** begins to lose weight at 250 °C, all the organic groups and coordinated waters are burned out after 756 °C. The final residuals may be Eu_2O_3, the observed total weight loss of 55.31% is close to the calculated one of 55.24%; **6** begins to lose weight at 185 °C, all the organic groups and coordinated waters are burned out after 845 °C. The final residuals may be Tb_4O_7; the observed total weight loss of 56.34% is compared to the calculated one of 54.16%; and the significant weight loss of **7** occurs after 285 °C and all the organic groups and coordinated waters are burned out after 696 °C. The final residuals may be Dy_2O_3. The observed total weight loss of 53.74% is close to the calculated one of 53.68%. The TG curves indicate that MOFs **1–7** would have good thermal stability up to 180 °C.

4. Conclusion

In summary, two types of new 3D rare earth MOFs have been synthesized by similar hydrothermal reactions of rare earth oxides with racemic tartaric acid. The frameworks of MOFs **1**, **4**,

5, **6** and **7** display **fsc**-3,4-*Iba*2 topology, while MOFs **2** and **3**, containing hydrophilic channels and triple helical chains, exhibit rare **fsx**-4,5-$P2_1/c$ topology. The TG curves indicate that these MOFs would have good thermal stability up to 180 °C. UV–vis spectrum property and luminescent property analyses indicated that MOFs **3**, **4**, **5**, **6**, **7** exhibit intense lanthanide characteristic photoluminescence at room temperature.

Acknowledgments

The authors are grateful to the Science and Technology Department of Zhejiang Province for financial support of the project (2007C21174).

Appendix A. Supporting information

Supplementary data associated with this article can be found in the online version at doi:10.1016/j.jssc.2011.11.012.

References

[1] (a) S. Noro, S. Kitagawa, M. Kondo, K. Seki, Angew. Chem. Int. Ed. 39 (2000) 2082;
(b) T.B. Dennis, D.C. Thomas, R.G. Juan, M.R. Ghadiri, Angew. Chem. Int. Ed. 40 (2001) 988;
(c) J. Zhang, Z.J. Li, Y. Kang, J.K. Cheng, Y.G. Yao, Inorg. Chem. 43 (2004) 8085;
(d) F. Michel, S. Torelli, F. Thomas, C. Duboc, C. Philouze, S. Hamman, E. Saint-Aman, J.L. Pierre, Angew. Chem. Int. Ed. 44 (2005) 438;
(e) D.L. Long, A.J. Blake, N.R. Champness, C. Wilson, M. Schröder, J. Am. Chem. Soc. 123 (2001) 3401;
(f) M. Cametti, M. Nissinen, A.D. Cort, L. Mandolini, K. Rissanen, J. Am. Chem. Soc. 127 (2005) 3831;
(g) A.J. Cairns, J.A. Perman, V. Kravtsov, L. Wojtas, V.Ch. Alkordi, M.H. Eddaoudi, M.J. Zaworotko, J. Am. Chem. Soc. 130 (2008) 1560;
(h) S.C. Xiang, W. Zhou, J.M. Gallegos, Y. Liu, B.L. Chen, J. Am. Chem. Soc. 131 (2009) 12415.
[2] (a) S.R. Seidel, P.J. Stang, Acc. Chem. Res. 35 (2002) 972;
(b) R.J. Hill, D.L. Long, N.R. Champness, P. Hubberstey, M. Schröder, Acc. Chem. Res. 38 (2005) 337;
(c) O.M. Yaghi, H. Li, T.L. Groy, J. Am. Chem. Soc. 118 (1996) 9096;
(d) M.L. Tong, S. Kitagawa, H.C. Chang, M. Ohba, Chem. Commun. (2004) 418;
(e) M. Dinca, A. Dailly, Y. Liu, C.M. Brown, J. Am. Chem. Soc. 128 (2006) 16876;
(f) S. Ma, D. Sun, J.M. Simmons, C.D. Collier, D. Yuan, H.C. Zhou, J. Am. Chem. Soc. 130 (2008) 1012;
(g) K. Koh, A.G. Wong-Foy, A.J. Matzger, J. Am. Chem. Soc. 131 (2009) 4184;
(h) N.L. Rosi, J. Eckert, M. Eddaoudi, D.T. Vodak, J. Kim, M. O'Keeffe, O.M. Yaghi, Science 300 (2003) 1127.
[3] (a) O.R. Evans, W. Lin, Acc. Chem. Res. 35 (2002) 511;
(b) C.S. Cundy, P.A. Cox, Chem. Rev. 103 (2003) 663;
(c) C. Volkringer, T. Loiseau, N. Guillou, G. Ferey, E. Elkaim, A. Vimont, Dalton Trans. (2009) 2241.
[4] (a) P. Amo-Ochoa, G. Givaja, P.J.S. Miguel, O. Castillo, F. Zamora, Inorg. Chem. Commun. 10 (2007) 921;
(b) D.W. Fu, W. Zhang, R.G. Xiong, Dalton Trans. (2008) 3946;
(c) M. Sabo, A. Henschel, H. Froede, E. Klemm, S. Kaskel, J. Mater. Chem. 17 (2007) 3827.
[5] (a) T. Loiseau, G.J. Ferey, Fluorine Chem. 128 (2007) 413;
(b) R.M. Wang, J. Zhang, L.J. Li, Inorg. Chem. 48 (2009) 7194;
(c) L. Zhang, J. Zhang, Z.J. Li, Y.Y. Qin, Q.P. Lin, Y.G. Yao, Chem-Eur. J. 15 (2009) 989.
[6] (a) R.G. Xiong, X. Xue, H. Zhao, X.Z. You, B.F. Abrahams, Z.L. Xue, Angew. Chem. Int. Ed. 41 (2002) 3800;
(b) M.L. Liu, M. Fang, B. Zhao, Z. Anorg. Allg. Chem. 635 (2009) 2592;
(c) G. Ferey, Chem. Mater. 13 (2001) 3084;
(d) K.C. Szeto, K.P. Lillerud, M. Tilset, M. Bjorgen, C. Prestipino, A. Zecchina, C. Lamberti, S. Bordiga, J. Phys. Chem. B 110 (2006) 21509;
(e) F.Q. Wang, W.H. Mu, X.J. Zheng, L.C. Li, D.C. Fang, L.P. Jin, Inorg. Chem. 47 (2008) 5225.
[7] (a) Y.H. He, Y.L. Feng, Y.Z. Lan, Y.H. Wen, Cryst. Growth Des. 8 (2008) 3586;
(b) X.H. Geng, Y.L. Feng, Y.Z. Lan, Inorg. Chem. Commun. 12 (2009) 447;
(c) Y.H. He, Y.Z. Lan, C.H. Zhan, Y.L. Feng, H. Su, Inorg. Chim. Acta 362 (2009) 1952;
(d) J.L. Yin, Y.L. Feng, Y.Z. Lan, Inorg. Chim. Acta 362 (2009) 3769;
(e) M.X. Jiang, C.H. Zhan, Y.L. Feng, Y.Z. Lan, Cryst. Growth Des. 10 (2010) 92;
(f) C.H. Zhan, M.X. Jiang, Y.L. Feng, J.W. Cheng, CrystEngComm 12 (2010) 420;
(g) Y.K. Lv, C.H. Zhan, Z.G. Jiang, Y.L. Feng, Inorg. Chem. Commun. 13 (2010) 440.
[8] (a) J.C.G. Bunzli, C. Piguet, Chem. Rev. 102 (2002) 1897;
(b) A.D. Dias, S. Viswanathan, Chem. Commun. (2004) 1024;
(c) T.K. Ronson, T. Lazarides, H. Adams, S.J.A. Pope, D. Sykes, S. Faulkner, S.J. Coles, M.B. Hursthouse, W. Clegg, R.W. Harrington, M.D. Ward, Chem-Eur J. 12 (2006) 9299.
[9] (a) C. Clavaguera, J.P. Dognon, P. Pyykko, Chem. Phys. Lett. 429 (2006) 8;
(b) I.D. Hughes, M. Dane, A. Ernst, W. Hergert, M. Luders, J. Poulter, J.B. Staunton, A. Svane, Z. Szotek, W.M. Temmerman, Nature 446 (2007) 650;
(c) L. Pan, X.Y. Huang, J. Li, Y.G. Wu, N.W. Zheng, Angew. Chem. Int. Ed. 39 (2000) 527.
[10] (a) C.D. Wu, C.Z. Lu, S.F. Lu, H.H. Zhuang, J.S. Huang, Dalton Trans. 3192 (2003);
(b) C.D. Wu, X.P. Zhan, C.Z. Lu, H.H. Zhuang, J.S. Huang, Acta Crystallogr. Sect. E 58 (2002) m228.
[11] S. Thushari, J.A.K. Cha, H.H.Y. Sung, S.S.Y. Chui, A.L.F. Leung, Y.F. Yen, I.D. Williams, Chem. Commun. (2005) 5515.
[12] M. Athar, G.H. Li, Z. Shi, Y. Chen, S.H. Feng, Solid State Sci. 10 (2008) 1853.
[13] P.F. Yan, J.C. Xing, G.M. Li, W.B. Sun, J.W. Zhang, G.F. Hou, J. Coord. Chem. 62 (2009) 2095.
[14] Y. Wang, G.X. Liu, Y.C. Chen, K.B. Wang, S.G. Meng, Inorg. Chim. Acta 363 (2010) 2668.
[15] (a) G.M. Sheldrick, SHELXS-97, Program for X-ray Crystal Structure Solution, University of Göttingen, Göttingen, Germany, 1997;
(b) G.M. Sheldrick, SHELXL-97, Program for X-Ray Crystal Structure Refinement, University of Göttingen, Göttingen, Germany, 1997.
[16] (a) G.E.M. Moussa, M.E. Shaban, F.A. Fouli, A.N. Hegazi, J. Chem. Soc. Pakistan 9 (1987) 239;
(b) J.B. McNair, Am. J. Bot. 23 (1936) 629;
(c) P. Thuery, Polyhedron 26 (2007) 101;
(d) M. Frisch, C.L. Cahill, Dalton Trans. (2005) 1518.
[17] (a) I.A. Kahwa, F.R. Fronczek, J. Selbin, Inorg. Chim. Acta 82 (1984) 167;
(b) O.E. Piro, E.E. Castellano, J.E. Baran, Z. Anorg. Allg. Chem. 628 (2002) 612;
(c) B. Yan, Q.Y. Xie, J. Coord. Chem. 56 (2003) 1285.
[18] (a) M. Nishiura, N. Okano, T. Imamoto, Bull. Chem. Soc. Jpn. 72 (1999) 1793;
(b) J.L. Sanz, R. Ruiz, A. Gleizes, A. Gleizes, F. Lloret, J. Faus, M. Julve, J.J. Borras-Almenar, Y. Journaux, Inorg. Chem. 35 (1996) 7384;
(c) C.M. Zaleski, A.D.C.V. Noord, J.M. Kampf, V.L. Pecoraro, Cryst. Growth Des. 7 (2007) 1098.
[19] (a) V.A. Blatov, TOPOS, A Multipurpose Crystallochemical Analysis with the Program Package, Russia, 2004;
(b) V.A. Blatov, Acta Cryst. A 63 (2007) 329;
(c) I.A. Baburin, V.A. Blatov, L. Carlucci, G. Cianib, D.M. Proserpio, CrystEng-Comm 10 (2008) 1822;
(d) V.A. Blatov, M.V. Peskov, Acta Crystallogr. Sect. B 62 (2006) 457;
(e) V.A. Blatov, D.M. Proserpio, Acta Cryst. A 63 (2009) 329;
(f) V.A. Blatov, L. Carlucci, G. Cianib, D.M. Proserpio, CrystEngComm 6 (2004) 377;
(g) I.A. Baburin, V.A. Blatov, L. Carlucci, G. Ciani, D.M. Proserpio, Cryst. Growth Des. 8 (2008) 519.
[20] (a) E. Hansson, J. Albertsson, Acta Chem. Scand. 22 (1968) 1682;
(b) W.J. Evans, D.G. Giarikos, M.A. Johnston, M.A. Greci, J.W. Ziller, Dalton Trans. (2002) 520;
(c) J.C. Trombe, A. Mohanu, Solid State Sci. 6 (2004) 1403;
(d) R.E. Marsh, Acta Crystallogr. Sect. B. 61 (2005) 359;
(e) W.J. Evans, D.G. Giarikos, J.W. Ziller, Organometallic 20 (2001) 5751.
[21] (a) N.W. Ockwig, O. Delagado-Friedrichs, M. O'Keeffe, O.M. Yaghi, J. Am. Chem. Soc. 38 (2005) 176;
(b) S.R. Batten, D.R. Turner, M.S. Neville, Coordination Polymers: Design, Analysis and Application RSC, Cambridge, 2009;
(c) L. Öhrström, K. Larsson, Dalton Trans. 3 (2004) 347;
(d) L. Öhrström, K. Larsson, Molecule-Based Materials. The Structural Network Approach, Elsevier, Amsterdam, 2005;
(e) M. O'Keeffe, M.A. Peskov, S.J. Ramsden, O.M. Yaghi, Acc. Chem. Res. 41 (2008) 1782;
(f) S.T. Hyde, O.D. Friedrichs, S.J. Ramsden, V. Robins, Solid State Sci. 8 (2006) 740;
(g) O.M. Yaghi, H. Li, C. Davis, D. Richardson, T.L. Groy, Acc. Chem. Res. 31 (1998) 474;
(h) A.F. Wells, Three-dimensional Nets and Polyhedra, Wiley, New York, 1977;
(i) A.F. Wells, Further Studies of Three-dimensional Nets, ACA Monograph 8, American Crystallographic Association, Buffalo, NY, 1979;
(j) M. O'Keeffe, S.T. Hyde, Zeolites 19 (1997) 370;
(k) M. O'Keeffe, Nature 400 (1999) 617;
(l) N.W. Ockwig, O.D. Friedrichs, M. O'Keeffe, O.M. Yaghi, Acc. Chem. Res. 38 (2005) 176.
[22] G.E.M. Moussa, M.E. Shaban, F.A. Fouli, A.N. Hegazi, J. Chem. Soc. Pakistan 9 (1987) 239.
[23] (a) R.S. Zhou, X.B. Cui, J.F. Song, X.Y. Xu, J.Q. Xu, T.G. Wang, J. Solid State Chem. 181 (2008) 2099;
(b) K.E. Gubina, J.A. Shatrava, V.A. Ovchynnikov, V.M. Amirkhanov, Polyhedron 19 (2000) 2203.
[24] (a) R.D. Peacock, Struct. Bonding (Berlin) 22 (1975) 83;
(b) G.H. Dieke, Spectra and Energy Levels of Rare Earth Ions in Crystals, Interscience Publishers, New York, 1968.
[25] L.H. Wang, W. Wang, W.G. Zhang, E.T. Kang, W. Huang, Chem. Mater. 12 (2000) 2212.
[26] (a) K.K. Mahato, A. Rai, S.B. Rai, Spectrochim. Acta Pt. a—Mol. Bio. 61 (2005) 431;
(b) M.D. Seltzer, A.O. Wright, C.A. Morrison, D.E. Wortman, J.B. Gruber, E.D. Filer, J. Phys. Chem. Solids 57 (1996) 1175.

[27] (a) C. Piguet, J.C.G. Bunzli, G. Bernardinelli, G. Hopfgartner, S. Petoud, O. Schaad, J. Am. Chem. Soc. 118 (1996) 6681;
(b) S.I. Klink, G.A. Hebbink, L. Grave, F. Van Veggel, D.N. Reinhoudt, L.H. Slooff, A. Polman, J.W. Hofstraat, J. Appl. Phys. 86 (1999) 1181.
[28] A.P. Bassett, S.W. Magennis, P.B. Glover, D.J. Lewis, N. Spencer, S. Parsons, R.M. Williams, L. De Cola, Z. Pikramenou, J. Am. Chem. Soc. 126 (2004) 9413.
[29] (a) Y.Q. Sun, J. Zhang, Y.M. Chen, G.Y. Yang, Angew. Chem. Int. Ed. 44 (2005) 5814;
(b) C.J. Li, M.X. Peng, J.D. Leng, M.M. Yang, Z. Lin, M.L. Tong, CrystEngComm 10 (2008) 1645.
[30] (a) T.M. Reineke, M. Eddaoudi, M. Fehr, D. Kelley, O.M. Yaghi, J. Am. Chem. Soc. 121 (1999) 1651;
(b) T. Terai, K. Kikuchi, S. Iwasawa, T. Kawabe, Y. Hirata, Y. Urano, T. Nagano, J. Am. Chem. Soc. 128 (2006) 6938.
[31] (a) J. Ye, J. Zhang, G. Ning, G. Tian, Y. Chen, Y. Wang, Cryst. Growth Des. 8 (2008) 3098;
(b) M.S. Liu, Q.Y. Yu, Y.P. Cai, C.Y. Su, X.M. Lin, X.X. Zhou, J.-W. Cai, Cryst. Growth Des. 8 (2008) 4083.